

# Polyoxometalate-Based Metal–Organic Frameworks with Conductive Polypyrrole for Supercapacitors

Hai-Ning Wang,<sup>†,‡</sup> Mi Zhang,<sup>‡</sup> A-Man Zhang,<sup>‡</sup> Feng-Cui Shen,<sup>‡</sup> Xiao-Kun Wang,<sup>‡</sup> Sheng-Nan Sun,<sup>‡</sup> Yong-Jun Chen,<sup>‡</sup> and Ya-Qian Lan<sup>\*,‡,§</sup>

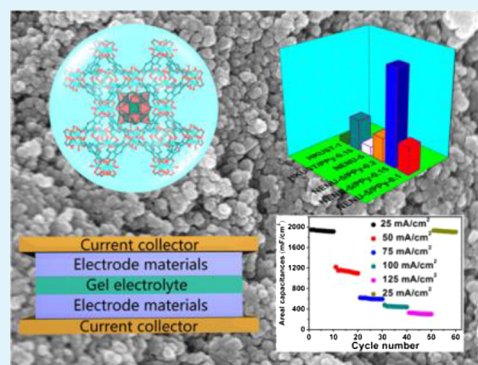
<sup>†</sup>School of Chemistry and Chemical Engineering, Shandong University of Technology, Zibo, Shandong 255049, P. R. China

<sup>‡</sup>Jiangsu Collaborative Innovation Centre of Biomedical Functional Materials, Jiangsu Key Laboratory of New Power Batteries, College of Chemistry and Materials Science, Nanjing Normal University, Nanjing, 210023, P. R. China

## Supporting Information

**ABSTRACT:** Metal–organic frameworks (MOFs) with high porosity could act as an ideal substitute for supercapacitors, but their poor electrical conductivities limit their electrochemical performances. In order to overcome this problem, conductive polypyrrole (PPy) has been introduced and a novel nanocomposite resulting from polyoxometalate (POM)-based MOFs (NENU-5) and PPy has been reported. It comprises the merits of POMs, MOFs, and PPy. Finally, the highly conductive PPy covering the surfaces of NENU-5 nanocrystallines can effectively improve the electron/ion transfer among NENU-5 nanocrystallines. The optimized NENU-5/PPy nanocomposite (the volume of Py is 0.15 mL) exhibits high specific capacitance ( $5147 \text{ mF}\cdot\text{cm}^{-2}$ ), larger than that of pristine NENU-5 ( $432 \text{ mF}\cdot\text{cm}^{-2}$ ). Furthermore, a symmetric supercapacitor device based on a NENU-5/PPy-0.15 nanocomposite possesses an excellent areal capacitance of  $1879 \text{ mF}\cdot\text{cm}^{-2}$ , which is far above other MOF-based supercapacitors.

**KEYWORDS:** polyoxometalate-based metal–organic frameworks, polyoxometalate, conductive polypyrrole, supercapacitor, synergetic effect



## 1. INTRODUCTION

Metal–organic frameworks (MOFs) are a kind of classic porous crystalline material with high surface area and porosity and widely explored in a wide range of research fields.<sup>1–10</sup> MOFs and their derivatives have been demonstrated their own values and functions in electrochemical energy storage and are receiving increasing interests in this field.<sup>11–14</sup> For example, Yaghi and his co-workers have covered a series of different hybrid materials based on MOFs, which act as supercapacitors, and several examples show high capacitances.<sup>15</sup> Simultaneously, polyoxometalates (POMs), as early transition-metal anionic clusters, have been widely explored in catalysis, electrochemistry, and energy conversion because of the following advantages: redox properties, stability, and diversity.<sup>16–21</sup> For example, theoretical and experimental approaches have demonstrated that  $[\text{PMo}_{12}\text{O}_{40}]^{3-}$  ( $\text{PMo}_{12}$ ) can act as an “electron sponge” because of its large electronic transfer capability.<sup>22</sup> Thus, if the advantages of MOFs and POMs are combined together, supercapacitors with high performance based on two types of materials might be achieved. Polyoxometalate-based MOFs (POMOFs) consist of both kinds of materials and may be attractive candidates for supercapacitors. Naturally, it is a very promising research field if employing POMOFs in preparing supercapacitors.

Polypyrrole (PPy), a class of typical conductive polymer, has acted as excellent electrode materials for supercapacitors.<sup>23–25</sup> In order to overcome the poor electrical conductivities of POMOFs and promote their applications in the field of supercapacitors, herein, we employ a simple approach to improve their overall electrical conductivity by using conductive PPy. Integrating POMOFs with PPy generates the nanocomposite, where POMOF particles can be effectively dispersed by PPy. As far as we know, no research results have been reported, which integrate MOFs, POMs, and PPy for supercapacitors. In this work, we combine the advantages of PPy and POMOFs to construct POMOF/PPy nanocomposites, where the conductivity case is determined and the excellent geometric characteristics of POMOFs are fully held. Among those reported POMOFs, NENU-5,<sup>26</sup> constructed from  $\text{PMo}_{12}$ , copper(II) acetate monohydrate, and 1,3,5-benzenetricarboxylate have been selected as a representative example because of its own features: (i)  $\text{PMo}_{12}$  as the “electron sponge” can accept a large number of electrons; (ii) encapsulating  $\text{PMo}_{12}$  into the MOF frameworks can effectively avoid its dissolution in the electrolyte and improve its

Received: July 19, 2018

Accepted: September 3, 2018

Published: September 3, 2018

electrochemical stability. Combining NENU-5 with pyrrole can give birth to nanocomposites (NENU-5/PPy). The nanocomposites have been explored for high-performance supercapacitors, which represents the first POMOF-based supercapacitor. In order to make full use of the advantages of this kind of nanocomposite, we also fabricate a symmetric all-solid-state supercapacitor, which shows high capacitance and superior cycling performance.

## 2. EXPERIMENTAL SECTION

**2.1. Chemical Substrates.** All purchased substrates were not purified and used directly, and deionized water was used in the process of experiments.

**2.2. Synthetic Section and Electrochemical Calculation.** The detailed experimental synthesis of materials and theoretical calculations are given in the [Supporting Information](#).

**2.3. Electrochemical Measurements.** The electrochemical tests were performed in a standard three-electrode system in 3 M KCl aqueous electrolyte at room temperature. The working electrodes were prepared by mixing the active electrode material (70%), carbon black (20%), and polyvinylidene difluoride (10%) in 1-methyl-2-pyrrolidinone, and then the obtained slurry was coated onto carbon cloth current collectors (1 cm × 2 cm). Finally, the electrode was dried in vacuum at 90 °C for 8 h. Meanwhile, the Pt foil and an Ag/AgCl electrode were used as the counter and reference electrodes, respectively. Cyclic voltammetry (CV), galvanostatic charge–discharge (GCD) measurements, and electrochemical impedance spectroscopy (EIS) were performed on a electrochemical workstation CHI 660D. The EIS data were collected with an ac voltage of 5 mV amplitude in the frequency range from 0.1 Hz to 100 kHz.

## 3. RESULTS AND DISCUSSION

In this communication, the synthetic route is briefly illustrated in [Figure 1](#) and the specific synthetic processes are given in the

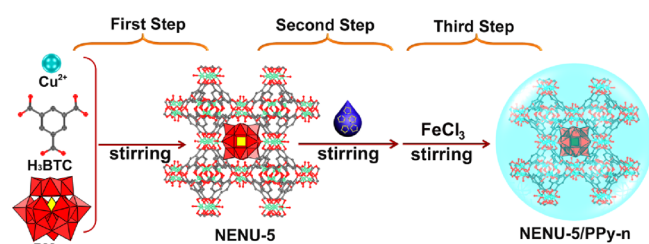


**Figure 1.** Schematic illustration of the synthetic process of NENU-5/PPy-*n*.

**Supporting Information.** First, NENU-5 nanocrystallines were synthesized in advance. Second, a certain volume of pyrrole was homogeneously dispersed in water under stirring, and then, the presynthesized NENU-5 nanocrystallines were added into the solution. Third, the iron trichloride hexahydrate, as the oxidant, was putted into the mixed system and used to catalyze the polymerization of pyrrole. Finally, the NENU-5/PPy nanocomposites were obtained after 8 h of reaction. In order to evaluate the impact of the PPy amount on the performance of the prepared nanocomposites, three NENU-5/PPy nanocomposites in the presence of different volumes of pyrrole monomers have been prepared, defined as NENU-5/PPy-*n* (*n* is the volume of pyrrole used in the synthesis process, 0.1, 0.15, and 0.2 mL are used). All prepared nanocomposites have been employed for supercapacitors. According to the experimental results, when the used pyrrole volume is 0.15 mL, the as-synthesized nanocomposite exhibits the best electrochemical performance, possessing an areal capacitance

of 5147 mF·cm<sup>-2</sup>. As the control experiment, we have also synthesized HKUST/PPy-0.15 via the same method, where the structure of HKUST-1 is isostructural to that of NENU-5 while without PMo<sub>12</sub> immobilized into its pores.

The structures of as-synthesized NENU-5 and HKUST-1 have been identified by powder X-ray diffraction (PXRD) patterns. Obviously, the PXRD patterns of the as-synthesized samples match well with their simulated patterns, demonstrating their phase purities ([Figures 2a](#) and [S1](#)). The compositions

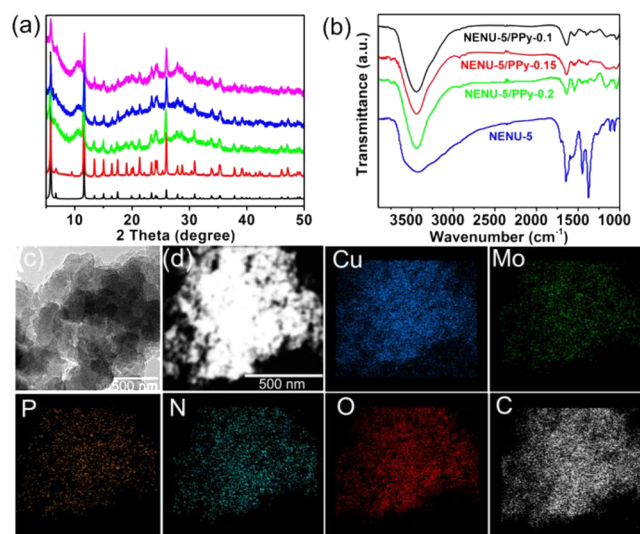


**Figure 2.** (a) Simulated XRD pattern of NENU-5 (black) and experimental XRD patterns of NENU-5 (red), NENU-5/PPy-0.1 (green), NENU-5/PPy-0.15 (blue), and NENU-5/PPy-0.2 (pink). (b) FTIR spectra of NENU-5/PPy-*n* and NENU-5. (c) TEM image of NENU-5/PPy-0.15. (d) Corresponding mapping images of Cu, Mo, P, N, O, and C.

of the prepared NENU-5/PPy-*n* and HKUST/PPy-0.15 have also been characterized by Fourier transform infrared (FTIR) and Raman spectra. The FTIR spectra of NENU-5/PPy-*n* are shown in [Figure 2b](#). These characteristic bands at about 1040, 1397, and 1547 cm<sup>-1</sup> in NENU-5/PPy-*n* are ascribed to the stretching vibrations of pyrrole ring groups.<sup>27–29</sup> Meanwhile, the FTIR spectra also demonstrate that PPy covers on the surface of HKUST-1 ([Figure S2](#)). In addition, the Raman spectra of NENU-5/PPy-0.15 and HKUST/PPy-0.15 also present characteristic bands of PPy at 1341, 1411, and 1578 cm<sup>-1</sup>, which are responsible for the C–N and C=C stretchings,<sup>29,30</sup> respectively, confirming the presence of PPy again ([Figures S3](#) and [S4](#)). Scanning electron microscopy (SEM) shows that the NENU-5/PPy-0.15 nanocomposites are objects with uniform shapes and average sizes smaller than 100 nm ([Figure S5](#)). The surfaces of NENU-5 are smooth, and after PPy incorporation, the surfaces of NENU-5/PPy-*n* become rougher and the intrinsic structure of NENU-5 is retained ([Figure 2a](#)). It should be mentioned that each nanocrystalline is covered by PPy, which serves as the hinge, facilitating electron/ion transport and making all nanocrystallines electroactive and interconnected. The transmission electron microscopy (TEM) image of NENU-5/PPy-0.15 nanocomposites has also been given ([Figure 2c](#)), and its energy-dispersive X-ray elemental mapping images prove that every element (C, N, O, P, Mo, and Cu) distributes uniformly ([Figure 2d](#)).



X-ray photoelectron spectra (XPS) of NENU-5/PPy-0.15 and HKUST/PPy-0.15 have been used to evaluate their compositions. As shown in Figure S6, the XPS spectrum of the sample NENU-5/PPy-0.15 has demonstrated the coexistence of C, N, O, Cu, P, and Mo elements. Three Gaussian peaks related to C–C/C=C, C–O, and C=O (284.3, 285.2, and 287.8 eV, respectively) have been presented in the XPS spectra of C 1s (Figure S6b).<sup>31</sup> The N 1s XPS spectra successfully confirm the generation of PPy (pyrrolic-N, about 400 eV) and could be divided into three peaks, which can be ascribed to –N= and –NH– segments (399.2 and 399.6 eV) in the backbone of PPy chains,<sup>32</sup> whereas the component corresponding to the peak at 400.6 eV belongs to the protonation states (–NH<sup>+</sup>–) (Figure S6c).<sup>33</sup> Two peaks at 232.3 and 235.4 eV may attribute to Mo<sup>6+</sup> 3d<sub>5/2</sub> and Mo<sup>6+</sup> 3d<sub>3/2</sub>, respectively (Figure S6d).<sup>34</sup> Furthermore, the Cu 2p spectrum has two main peaks of Cu 2p<sub>3/2</sub> at the binding of 933.5 eV and Cu 2p<sub>1/2</sub> at the binding of 955.4 eV, and they can clearly demonstrate the existence of Cu<sup>2+</sup> (Figure S6e).<sup>35</sup> The O 1s spectra reveal the co-existence of C–O (532.3 eV) and C=O (531 eV) (Figure S6f). Additionally, we also measure the XPS spectrum of the as-synthesized HKUST/PPy-0.15, which demonstrates the co-existence of C, O, N, and Cu elements (Figure S7). The porosities of NENU-5/PPy-*n* and HKUST/PPy-0.15 nanocomposites have been evaluated using N<sub>2</sub> adsorption–desorption measurements (Figure S8). The experimental results reveal that the specific surface areas of NENU-5/PPy-*n* increase in turn (21.57, 50.72, and 104.64 m<sup>2</sup> g<sup>–1</sup>), whereas HKUST/PPy-0.15 possesses the specific surface area 31.29 m<sup>2</sup> g<sup>–1</sup>.

The electrochemical performances of six electrode materials have been first studied by CV in a three-electrode system using KCl solution (3 mol/L) as the electrolyte, which is operated with a potential window range of –0.1–0.8 V at different scan rates (Figures 3a and S9). At the same scan rate (10 mV/s), diverse areas are reflected by CV curves of different electrode materials. The CV area of NENU-5/PPy-0.15 reaches the maximum, indicating that when the pyrrole volume is 0.15 mL, the prepared electrode material NENU-5/PPy-0.15 possesses

the best performance. When the pyrrole volume is 0.1/0.2 mL, the decreases of CV areas occur, implying that the performances of corresponding electrode materials are lower than that of NENU-5/PPy-0.15. The experimental results mean that the less/excess PPy cannot effectively promote the charge/ion transfer. Moreover, the CV curves of six electrode materials at other scan rates are given in the Supporting Information (Figure S9).

Areal capacitance is one of the key parameters, which reflects the electrochemical performances of the electrode materials. Maximum areal capacitances of 1354, 5147, and 1383 mF·cm<sup>–2</sup> for NENU-5/PPy-0.1/0.15/0.2 electrode materials have been obtained at the scan rate of 10 mV·s<sup>–1</sup>, respectively (Figure 3b). Moreover, HKUST/PPy-0.15, NENU-5, and HKUST-1 show areal capacitances of 2243, 432, and 358 mF·cm<sup>–2</sup> at the same scan rate (Figure 3b). Obviously, compared with HKUST/PPy-0.15, the introduction of PMo<sub>12</sub> indeed improves the specific capacitance of the electrode materials. Maximum areal capacitances for NENU-5/PPy-*n*, HKUST/PPy-0.15, NENU-5, and HKUST-1 electrode materials have also been obtained at different scan rates of 20, 50, 100, 200, and 500 mV·s<sup>–1</sup> (Figure S10). For NENU-5/PPy-0.15, its gravimetric capacitance is 779.8 F·g<sup>–1</sup> at 10 mV·s<sup>–1</sup>, far superior to those of NENU-5/PPy-0.1 (281.9 F·g<sup>–1</sup>), NENU-5/PPy-0.2 (244.3 F·g<sup>–1</sup>), HKUST/PPy-0.15 (366.5 F·g<sup>–1</sup>), NENU-5 (86.4 F·g<sup>–1</sup>), and HKUST-1 (71.6 F·g<sup>–1</sup>). As far as we know, this value is higher than those of other MOF-based materials, as shown in Table S1. The aforementioned experimental results show that the appropriate surface areas and porosities, as well as good conductivities, facilitate electron or ion transport, resulting in the improvement of the electrochemical performance. This phenomenon indicates that the components and microstructures have a great influence on the performance of electrode materials.

Additionally, the specific capacities of six electrode materials under different current densities are also calculated by means of the GCD curves. The curves of NENU-5/PPy-0.15 show a typical shape of pseudocapacitive behavior. Similar to CV curves, the NENU-5/PPy-0.15 still reveals the longest discharge time (Figure S11) and shows the specific capacity (1090 mF·cm<sup>–2</sup>) at a current density of 0.5 mA·cm<sup>–2</sup>. The specific capacities of others exhibit 313, 277, 108, 353, and 57 mF·cm<sup>–2</sup> at the same current density (Figure 3c). The GCD curves obtained at the different charging and discharging rates from 1, 1.5, 2 to 2.5 mA·cm<sup>–2</sup> have also been given (Figures 3d and S11). Furthermore, the cycling stability of NENU-5/PPy-0.15 has been performed (Figure S12). Figure S13 shows the Nyquist plots of six electrode materials at open-circuit potential. The charge-transfer resistance (*R*<sub>ct</sub>) value of NENU-5/PPy-0.15 is smaller than those of other nanocomposites. The experimental results indicate that the introduction of PPy is in favor of speeding up the charge transfer. When the volume of pyrrole is lower/above than 0.15 mL, the specific capacities decrease, implying that the PPy constructed by 0.15 mL pyrrole might be beneficial to the charges/ions diffusing into the inner NENU-5.

Compared with the performances of other nanocomposites, the higher performance of the NENU-5/PPy composites can be ascribed to the following reasons: (i) PMo<sub>12</sub> inside the framework takes part in redox reactions and provides pseudocapacitance because of the transformation of Mo (Mo<sup>6+</sup> to Mo<sup>4+</sup>), and its function has been confirmed by XPS results (Figure S14) and reported examples as well as the

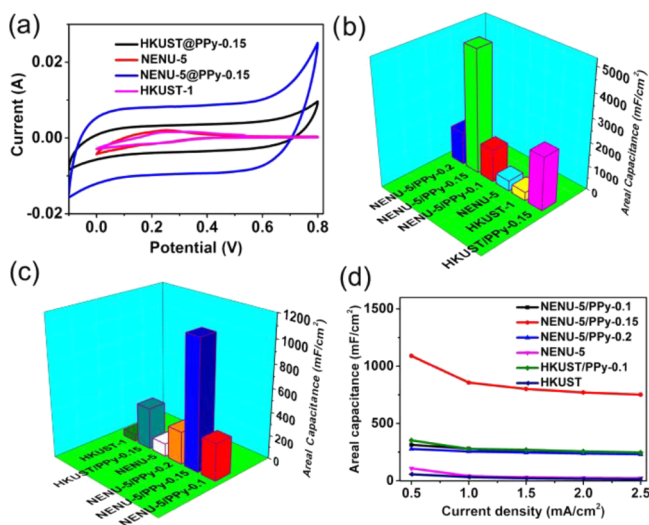


**Figure 3.** (a) CV curves at 10 mV·s<sup>–1</sup>. (b) Maximum areal capacitances at 10 mV·s<sup>–1</sup>. (c) Areal capacitances calculated by GCD curves at a current density of 0.5 mA·cm<sup>–2</sup>. (d) Calculated areal capacitances at various current densities.

comparison of capacitances between NENU-5/PPy-0.15 and HKUST/PPy-0.15;<sup>18,21</sup> (ii) on one hand, PPy can improve the conductivity of materials greatly and promote electron transfer, on the other hand, they restrain the volume change of NENU-5 and enhance the structural stability during the charge/discharge process;<sup>29,36</sup> (iii) MOFs with rich access channels and micropores not only disperse  $\text{PMo}_{12}$  uniformly and stop  $\text{PMo}_{12}$  from dissolving in the electrolyte but also act as an electrochemical double layer capacitor, in favor of charge storage/transport and the ionic diffusion;<sup>21,37</sup> (iv) the  $\pi$ - $\pi$  conjugations between MOFs and pyrrole not only facilitate the polymerization of pyrrole on the surface of MOFs but also devotes for a remarkable improvement of electrochemical performance; and (v) the small sizes of nanocomposites (demonstrated by the SEM images) could promote the transport of electrolyte ions. The schematic diagram of the possible mechanism is shown in Figure 4.

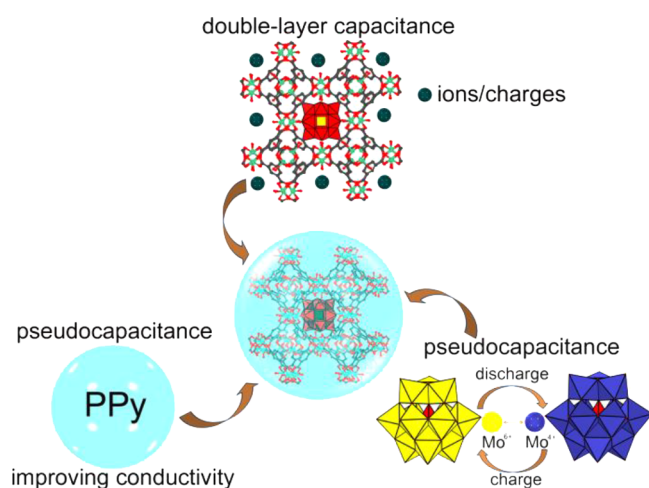


**Figure 4.** Scheme of possible mechanism for the cooperative capacity of NENU-5/PPy-0.15.

Furthermore, we fabricate a symmetric all-solid-state supercapacitor device. The same two pieces of NENU-5/PPy-0.15 electrodes with an area of  $1 \times 2 \text{ cm}^2$  are parallelly placed, and  $\text{H}_2\text{SO}_4/\text{poly}(\text{vinyl alcohol})$  is used as the separator and the solid electrolyte (Figure 5a). The device's effective area is approximately  $2.0 \text{ cm}^2$ . The CV has been first used to study its electrochemical behaviors in the range of  $-0.1$ – $0.8 \text{ V}$  with the scan rates between  $10$  and  $500 \text{ mV s}^{-1}$  (Figure 5b). To further evaluate its electrochemical performance, GCD measurements at relatively high current densities from  $25$  to  $125 \text{ mA cm}^{-2}$  are carried out. With the increased current density, this solid device shows decreased specific capacitance. The areal specific capacitances of this device are  $1879$ ,  $1250$ ,  $607$ ,  $436$ , and  $295 \text{ mF cm}^{-2}$  at different current densities (Figure 5c) and decrease as the currents increase. The experimental phenomenon may be attributable to the incomplete redox reactions because of the poor connection between the electrochemical system and the increased current.<sup>38</sup> The energy densities ( $E$ ) are  $0.316$ ,  $0.210$ ,  $0.102$ ,  $0.0733$ , and  $0.0496 \text{ mW h cm}^{-2}$  with power densities ( $P$ ) of  $6.4$ ,  $15.62$ ,  $18.17$ ,  $29.3$ , and  $52.5 \text{ mW cm}^{-2}$ , respectively, which reveal that the device maybe have potential applications in energy storage. The relationships between energy densities and power densities under various current densities are given in Ragone plots (Figure 5d). Additionally, the performance of this device exceeds the values

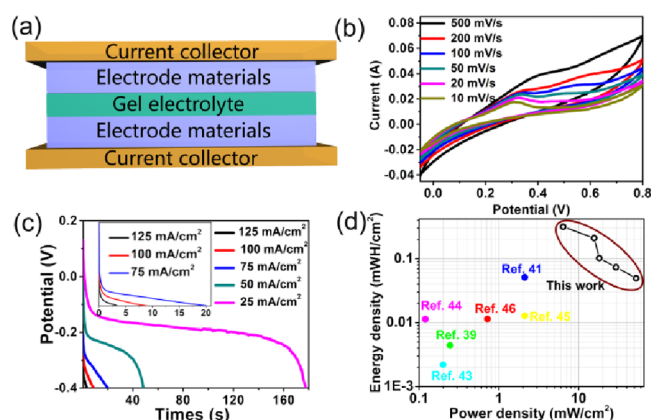


**Figure 5.** (a) Schematic diagram of a supercapacitor device based on NENU-5/PPy-0.15 electrode material and gel electrolyte. (b) CV curves measured at different scan rates. (c) GCD curves measured at different current densities. Inset: GCD curves at  $75$ ,  $100$ , and  $125 \text{ mA cm}^{-2}$ . (d) Ragone plots of the device and comparisons of data covered by the literatures.

achieved for other MOF-based supercapacitors.<sup>39–46</sup> More importantly, the device exhibits good cycling performance. When the current densities increase from  $25$  to  $125 \text{ mA cm}^{-2}$  and then back to the original current, the capacity can still maintain the original value without a noticeable decrease (Figure S15). It should be noted that the cycling stability of this device has also been measured (Figure S16).

## 4. CONCLUSIONS

In summary, the NENU-5/PPy-0.15 exhibits excellent electrochemical performance because of its following characteristics: good electroconductivity, appropriate surface area, porosity, and rich active sites. NENU-5/PPy-0.15 shows high specific capacitance about  $5147 \text{ mF cm}^{-2}$ , larger than that of pristine NENU-5. Meanwhile, a symmetric supercapacitor device based on NENU-5/PPy-0.15 has been successfully developed, which exhibits areal specific capacitance  $1879 \text{ mF cm}^{-2}$ , and is far above other MOF-based supercapacitors. This work provides a new strategy to prepare MOF-based supercapacitors and extends the diversity of the supercapacitor family.

## ■ ASSOCIATED CONTENT

### Supporting Information

The Supporting Information is available free of charge on the ACS Publications website at DOI: 10.1021/acsami.8b12194.

Detailed experimental process; the morphology and component analysis of NENU-5/PPy- $n$  and HKUST/PPy-0.15; electrochemical data of NENU-5/PPy- $n$ , NENU-5, HKUST-1 and HKUST/PPy-0.15; and electrochemical tests of the solid device (PDF)

## ■ AUTHOR INFORMATION

### Corresponding Author

\*E-mail: yqlan@nynu.edu.cn.

### ORCID

Ya-Qian Lan: 0000-0002-2140-7980

### Author Contributions

The manuscript was written through contributions of all authors. All authors have given approval to the final version of the manuscript.

## Notes

The authors declare no competing financial interest.

## ACKNOWLEDGMENTS

The authors are grateful to the financial aid from the National Natural Science Foundation of China (no. 21601109) and the China Postdoctoral Science Foundation (no. 2018M632328).

## REFERENCES

- (1) Meng, X.; Wang, H.-N.; Song, S.-Y.; Zhang, H.-J. Proton-conducting crystalline porous materials. *Chem. Soc. Rev.* **2017**, *46*, 464–480.
- (2) Lustig, W. P.; Mukherjee, S.; Rudd, N. D.; Desai, A. V.; Li, J.; Ghosh, S. K. Metal-organic frameworks: functional luminescent and photonic materials for sensing applications. *Chem. Soc. Rev.* **2017**, *46*, 3242–3285.
- (3) Liu, J.; Wöll, C. Surface-supported metal-organic framework thin films: fabrication methods, applications, and challenges. *Chem. Soc. Rev.* **2017**, *46*, S730–S770.
- (4) Stassen, I.; Burtch, N.; Talin, A.; Falcaro, P.; Allendorf, M.; Ameloot, R. An updated roadmap for the integration of metal-organic frameworks with electronic devices and chemical sensors. *Chem. Soc. Rev.* **2017**, *46*, 3185–3241.
- (5) Du, D.-Y.; Qin, J.-S.; Li, S.-L.; Su, Z.-M.; Lan, Y.-Q. Recent advances in porous polyoxometalate-based metal-organic framework materials. *Chem. Soc. Rev.* **2014**, *43*, 4615–4632.
- (6) Rogge, S. M. J.; Bavykina, A.; Hajek, J.; Garcia, H.; Olivos-Suarez, A. I.; Sepúlveda-Escribano, A.; Vimont, A.; Clet, G.; Bazin, P.; Kapteijn, F.; Daturi, M.; Ramos-Fernandez, E. V.; Llabrés i Xamena, F. X.; Van Speybroeck, V.; Gascon, J. Metal-organic and covalent organic frameworks as single-site catalysts. *Chem. Soc. Rev.* **2017**, *46*, 3134–3184.
- (7) Bobbitt, N. S.; Mendonca, M. L.; Howarth, A. J.; Islamoglu, T.; Hupp, J. T.; Farha, O. K.; Snurr, R. Q. Metal-organic frameworks for the removal of toxic industrial chemicals and chemical warfare agents. *Chem. Soc. Rev.* **2017**, *46*, 3357–3385.
- (8) Lian, X.; Fang, Y.; Joseph, E.; Wang, Q.; Li, J.; Banerjee, S.; Lollar, C.; Wang, X.; Zhou, H.-C. Enzyme-MOF (metal-organic framework) composites. *Chem. Soc. Rev.* **2017**, *46*, 3386–3401.
- (9) Zhou, J.; Wang, B. Emerging crystalline porous materials as a multifunctional platform for electrochemical energy storage. *Chem. Soc. Rev.* **2017**, *46*, 6927–6945.
- (10) Li, S.-L.; Xu, Q. Metal-organic frameworks as platforms for clean energy. *Energy Environ. Sci.* **2013**, *6*, 1656–1683.
- (11) Miao, M.; Pan, J.; He, T.; Yan, Y.; Xia, B. Y.; Wang, X. Molybdenum Carbide-Based Electrocatalysts for Hydrogen Evolution Reaction. *Chem.—Eur. J.* **2017**, *23*, 10947–10961.
- (12) Pan, J.; Xu, Y. Y.; Yang, H.; Dong, Z.; Liu, H.; Xia, B. Y. Advanced Architectures and Relatives of Air Electrodes in Zn-Air Batteries. *Adv. Sci.* **2018**, *5*, 1700691.
- (13) Zheng, S.; Li, X.; Yan, B.; Hu, Q.; Xu, Y.; Xiao, X.; Xue, H.; Pang, H. Transition-Metal (Fe, Co, Ni) Based Metal-Organic Frameworks for Electrochemical Energy Storage. *Adv. Energy Mater.* **2017**, *7*, 1602733.
- (14) Wang, F.; Wu, X.; Yuan, X.; Liu, Z.; Zhang, Y.; Fu, L.; Zhu, Y.; Zhou, Q.; Wu, Y.; Huang, W. Latest advances in supercapacitors: from new electrode materials to novel device designs. *Chem. Soc. Rev.* **2017**, *46*, 6816–6854.
- (15) Choi, K. M.; Jeong, H. M.; Park, J. H.; Zhang, Y.-B.; Kang, J. K.; Yaghi, O. M. Supercapacitors of Nanocrystalline Metal-Organic Frameworks. *ACS Nano* **2014**, *8*, 7451–7457.
- (16) Ji, Y.; Huang, L.; Hu, J.; Streb, C.; Song, Y.-F. Polyoxometalate-functionalized nanocarbon materials for energy conversion, energy storage and sensor systems. *Energy Environ. Sci.* **2015**, *8*, 776–789.
- (17) Chen, J.-J.; Symes, M. D.; Fan, S.-C.; Zheng, M.-S.; Miras, H. N.; Dong, Q.-F.; Cronin, L. High-Performance Polyoxometalate-Based Cathode Materials for Rechargeable Lithium-Ion Batteries. *Adv. Mater.* **2015**, *27*, 4649–4654.
- (18) Nishimoto, Y.; Yokogawa, D.; Yoshikawa, H.; Awaga, K.; Irle, S. Super-Reduced Polyoxometalates: Excellent Molecular Cluster Battery Components and Semipermeable Molecular Capacitors. *J. Am. Chem. Soc.* **2014**, *136*, 9042–9052.
- (19) Chen, Y.; Han, M.; Tang, Y.; Bao, J.; Li, S.; Lan, Y.; Dai, Z. Polypyrrole-polyoxometalate/reduced graphene oxide ternary nano-hybrids for flexible, all-solid-state supercapacitors. *Chem. Commun.* **2015**, *51*, 12377–12380.
- (20) Suárez-Guevara, J.; Ruiz, V.; Gómez-Romero, P. Stable graphene–polyoxometalate nanomaterials for application in hybrid supercapacitors. *Phys. Chem. Chem. Phys.* **2014**, *16*, 20411–20414.
- (21) Wei, T.; Zhang, M.; Wu, P.; Tang, Y.-J.; Li, S.-L.; Shen, F.-C.; Wang, X.-L.; Zhou, X.-P.; Lan, Y.-Q. POM-based metal-organic framework/reduced graphene oxide nanocomposites with hybrid behavior of battery-supercapacitor for superior lithium storage. *Nano Energy* **2017**, *34*, 205–214.
- (22) Wang, H.; Hamanaka, S.; Nishimoto, Y.; Irle, S.; Yokoyama, T.; Yoshikawa, H.; Awaga, K. In Operando X-ray Absorption Fine Structure Studies of Polyoxometalate Molecular Cluster Batteries: Polyoxometalates as Electron Sponges. *J. Am. Chem. Soc.* **2012**, *134*, 4918–4924.
- (23) Snook, G. A.; Kao, P.; Best, A. S. Conducting-polymer-based supercapacitor devices and electrodes. *J. Power Sources* **2011**, *196*, 1–12.
- (24) Ji, W.; Ji, J.; Cui, X.; Chen, J.; Liu, D.; Deng, H.; Fu, Q. Polypyrrole encapsulation on flower-like porous NiO for advanced high-performance supercapacitors. *Chem. Commun.* **2015**, *51*, 7669–7672.
- (25) Kuwabata, S.; Nakamura, J.; Yoneyama, H. Dependence of Conductivity of Polypyrrole Film Doped with p-Phenol Sulfonate on Solution pH. *J. Electrochem. Soc.* **1990**, *137*, 2147.
- (26) Sun, C.-Y.; Liu, S.-X.; Liang, D.-D.; Shao, K.-Z.; Ren, Y.-H.; Su, Z.-M. Highly Stable Crystalline Catalysts Based on a Microporous Metal–Organic Framework and Polyoxometalates. *J. Am. Chem. Soc.* **2009**, *131*, 1883–1888.
- (27) Bashid, H. A. A.; Lim, H. N.; Kamaruzaman, S.; Rashid, S. A.; Yunus, R.; Huang, N. M.; Yin, C. Y.; Rahman, M. M.; Altarawneh, M.; Jiang, Z. T.; Alagarsamy, P. Electrodeposition of Polypyrrole and Reduced Graphene Oxide onto Carbon Bundle Fiber as Electrode for Supercapacitor. *Nanoscale Res. Lett.* **2017**, *12*, 246–256.
- (28) Su, N.; Li, H. B.; Yuan, S. J.; Yi, S. P.; Yin, E. Q. Synthesis and characterization of polypyrrole doped with anionic spherical polyelectrolyte brushes. *Express Polym. Lett.* **2012**, *6*, 697–705.
- (29) Jiao, Y.; Chen, G.; Chen, D.; Pei, J.; Hu, Y. Bimetal-organic framework assisted polymerization of pyrrole involving air oxidant to prepare composite electrodes for portable energy storage. *J. Mater. Chem. A* **2017**, *5*, 23744–23752.
- (30) Jian, X.; Yang, H.-m.; Li, J.-g.; Zhang, E.-h.; Cao, L.-l.; Liang, Z.-h. Flexible all-solid-state high-performance supercapacitor based on electrochemically synthesized carbon quantum dots/polypyrrole composite electrode. *Electrochim. Acta* **2017**, *228*, 483–493.
- (31) Hu, J.; Diao, H.; Luo, W.; Song, Y.-F. Dawson-Type Polyoxomolybdate Anions ( $P_2Mo_{18}O_{62}^{26-}$ ) Captured by Ionic Liquid on Graphene Oxide as High-Capacity Anode Material for Lithium-Ion Batteries. *Chem.—Eur. J.* **2017**, *23*, 8729–8735.
- (32) Wallace, G. G.; Teasdale, P. R.; Spinks, G. M. *Conductive Electroactive Polymers: Intelligent Polymer Systems*; CRC Press: Boca Raton, FL, USA, 2008.
- (33) Boota, M.; Paranthaman, M. P.; Naskar, A. K.; Li, Y.; Akato, K.; Gogotsi, Y. Waste Tire Derived Carbon-Polymer Composite Paper as Pseudocapacitive Electrode with Long Cycle Life. *ChemSusChem* **2015**, *8*, 3576–3581.
- (34) Xie, J.; Zhang, Y.; Han, Y.; Li, C. High-Capacity Molecular Scale Conversion Anode Enabled by Hybridizing Cluster-Type Framework of High Loading with Amino-Functionalized Graphene. *ACS Nano* **2016**, *10*, 5304–5313.
- (35) Wang, C.; Zhu, J.; Liang, S.; Bi, H.; Han, Q.; Liu, X.; Wang, X. Reduced graphene oxide decorated with CuO-ZnO hetero-junctions:



towards high selective gas-sensing property to acetone. *J. Mater. Chem. A* **2014**, *2*, 18635–18643.

(36) Yang, C.; Shi, M.; Song, X.; Zhao, X.; Zhao, L.; Liu, J.; Zhang, P.; Gao, L. A robust hierarchical microcapsule for efficient supercapacitors exhibiting an ultrahigh current density of 300 A·g<sup>-1</sup>. *J. Mater. Chem. A* **2018**, *6*, 5724–5732.

(37) Wang, L.; Han, Y.; Feng, X.; Zhou, J.; Qi, P.; Wang, B. Metal-organic frameworks for energy storage: Batteries and supercapacitors. *Coord. Chem. Rev.* **2016**, *307*, 361–381.

(38) Wang, L.; Yang, H.; Pan, G.; Miao, L.; Chen, S.; Song, Y. Polyaniline-Carbon Nanotubes@Zeolite Imidazolate Framework 67-Carbon Cloth Hierarchical Nanostructures for Supercapacitor Electrode. *Electrochim. Acta* **2017**, *240*, 16–23.

(39) Wang, L.; Feng, X.; Ren, L.; Piao, Q.; Zhong, J.; Wang, Y.; Li, H.; Chen, Y.; Wang, B. Flexible Solid-State Supercapacitor Based on a Metal-Organic Framework Interwoven by Electrochemically-Deposited PANI. *J. Am. Chem. Soc.* **2015**, *137*, 4920–4923.

(40) Sheberla, D.; Bachman, J. C.; Elias, J. S.; Sun, C.-J.; Shao-Horn, Y.; Dincă, M. Conductive MOF Electrodes for Stable Supercapacitors with High Areal Capacitance. *Nat. Mater.* **2017**, *16*, 220–224.

(41) Fu, D.; Li, H.; Zhang, X.-M.; Han, G.; Zhou, H.; Chang, Y. Flexible solid-state supercapacitor fabricated by metal-organic framework/graphene oxide hybrid interconnected with PEDOT. *Mater. Chem. Phys.* **2016**, *179*, 166–173.

(42) Zhang, Y.-Z.; Cheng, T.; Wang, Y.; Lai, W.-Y.; Pang, H.; Huang, W. A Simple Approach to Boost Capacitance: Flexible Supercapacitors Based on Manganese Oxides@MOFs via Chemically Induced In Situ Self-Transformation. *Adv. Mater.* **2016**, *28*, 5242–5248.

(43) Fu, D.; Zhou, H.; Zhang, X.-M.; Han, G.; Chang, Y.; Li, H. Flexible solid-state supercapacitor of metal-organic framework coated on carbon nanotube film interconnected by electrochemically-codeposited PEDOT-GO. *ChemistrySelect* **2016**, *1*, 285–289.

(44) Xu, X.; Tang, J.; Qian, H.; Hou, S.; Bando, Y.; Hossain, M. S. A.; Pan, L.; Yamauchi, Y. Three-Dimensional Networked Metal-Organic Frameworks with Conductive Polypyrrole Tubes for Flexible Supercapacitors. *ACS Appl. Mater. Interfaces* **2017**, *9*, 38737–38744.

(45) Qi, K.; Hou, R.; Zaman, S.; Qiu, Y.; Xia, B. Y.; Duan, H. Construction of Metal-Organic Framework/Conductive Polymer Hybrid for All-Solid-State Fabric Supercapacitor. *ACS Appl. Mater. Interfaces* **2018**, *10*, 18021–18028.

(46) Qi, K.; Hou, R.; Zaman, S.; Xia, B. Y.; Duan, H. A core/shell structured tubular graphene nanoflake-coated polypyrrole hybrid for all-solid-state flexible supercapacitors. *J. Mater. Chem. A* **2018**, *6*, 3913–3918.